Manuscript prepared for Atmos. Chem. Phys.
with version 5.0 of the LaTeX class copernicus.cls.
Date: 28 August 2014

# On the impact of the temporal variability of the collisional quenching process on the mesospheric OH emission layer: A study based on SD-WACCM4 and SABER

S. Kowalewski[1], C. von Savigny[2], M. Palm[1], I.C. McDade[3], and J. Notholt[1]

[1]Institute of Environmental Physics, University of Bremen, Bremen, Germany
[2]Institute of Physics, Ernst-Moritz-Arndt-University of Greifswald, Greifswald, Germany
[3]Department of Earth and Space Science & Engineering, York University, Toronto, Canada

*Correspondence to:* Stefan Kowalewski
kowalewsi@iup.physik.uni-bremen.de

**Abstract.**

The mesospheric OH Meinel emissions are subject of many theoretical and observational studies devoted to this part of the atmosphere. Depending on the initial vibrational level of excitation the altitude of the considered OH Meinel emission is systematically shifted, which has important implications for the intercomparison of different studies considering different transition bands. Previous model studies suggest that these vertical shifts are essentially caused by the process of collisional quenching with atomic oxygen. Following this hypothesis, a recent study found experimental evidence of a coherent seasonality at tropical latitudes between vertical shifts of different OH Meinel bands and changes in atomic oxygen concentrations. Despite the consistent finding to the above mentioned hypothesis, it cannot be excluded that the actual temporal variability of the vertical shifts between different OH Meinel bands may in addition be controlled or even dominated by other processes. It remains an open question whether the observed temporal evolution is indeed mainly controlled by the modulation of the collisional quenching process with atomic oxygen. By means of a sensitivity study which employs a quenching model to simulations made with the SD-WACCM4 chemistry climate model, we aim at assessing this question. From this study we find that the observed seasonality of vertical OH Meinel shifts is only partially controlled by temporal changes in atomic oxygen concentrations, while molecular oxygen has another noticeable impact on the vertical OH Meinel shifts. This in particular becomes evident for the diurnal variability of vertical OH Meinel shifts, which reveal only a poor correlation with the atomic oxygen species. In addition, changes in the $H + O_3$ source gases provide another mechanism that can potentially affect the diurnal variability in addition. By comparison with limb radiance observations from the SABER/TIMED

satellite this provides an explanation for the less evident diurnal response between changes in O concentrations and vertical OH Meinel shifts. On the other hand, at seasonal time scales the coherency between both quantities is again evident in SABER/TIMED but less pronounced compared to our model simulations.

## 1 Introduction

The hydroxyl (OH) emission layer is a prominent feature of the mesopause region. Its main production process is commonly referred to as the Bates–Nicolet mechanism (McDade, 1991). This mechanism suggests the exothermic reaction between $O_3$ and H, which leads to rotational-vibrationally excited OH radicals (Bates and Nicolet, 1950). According to the available exothermic energy of this reaction, these radicals can have excited vibrational states up to the $\nu = 9$ quantum number. Lower vibrational states can be populated via spontaneous emission, but also through collisional quenching with ambient species. Hence, we can distinguish between different OH($\nu$) layers with respect to their vibrational excitation states.

Because different observational studies on the mesospheric OH Meinel emission rely on different transition bands, it is of general interest to understand systematic differences between the vertical profiles of the associated OH($\nu$) layers. As we know from previous rocket campaigns (e.g. see Baker and Stair Jr (1988) for a comprehensive compilation of rocket campaigns), systematic vertical shifts exist between these layers, while further studies have shown that collisional quenching with ambient species is significantly affecting these shifts (e.g. Dodd et al., 1994; Makhlouf et al., 1995, and Adler-Golden, 1997). In particular atomic oxygen is an effective quencher and its impact on the vertical distribution of different OH($\nu$) layers has been recently investigated by von Savigny et al. (2012). Based on a sensitivity study, which relies on an updated version of a quenching model by McDade (1991), they suggest that quenching with atomic oxygen causes an upward shift of the individual OH($\nu$) layers with increasing vibrational state. In a follow-up study von Savigny and Lednyts'kyy (2013) provided experimental evidence that the vertical shifts between different OH bands are indeed correlated with the amount of atomic oxygen in the altitude range of the OH emission layer. Despite the consistent findings between both studies, it should be outlined that the simulated OH profiles by von Savigny et al. (2012) were limited to a single month based on the MSIS climatology, while the effect of collisional O quenching has been considered by different scaling factors in the associated rate term. On the other hand, systematic changes in the vertical $O_3$ and H profiles will also affect the temporal variability of the vertical OH($\nu$) shifts and must be taken into account when discussing the impact of collisional quenching on the vertical structure of the OH($\nu$) layers. Thus, it remains an open question whether the temporal changes in the relative vertical OH($\nu$) shifts are mainly driven by the temporal variability of the ambient quenching species, the source gases of OH or by a combination of both.

To investigate the importance of the temporal variability of the collisional quenching on the vertical OH($\nu$) shifts, this study established an updated quenching model that is applied to simulations made with the Whole Atmosphere Community Climate Model driven with Specified Dynamical fields (SD-WACCM4).

The emphasis of this study will be on the equatorial regions, where the large amplitude of the diurnal migrating tide has a strong impact on OH airglow and ambient temperatures (Shepherd et al., 2006). Many studies have reported evidence of a semi-annual oscillation in airglow observations that is associated with the large seasonal changes in the tidal amplitude. For instance, Marsh et al. (2006) show a pronounced semi-annual oscillation in SABER OH Volume-Emission-Rate (VER) measurements at equatorial latitudes. A similar seasonality was also recently shown for OH VER measurements from SCIAMACHY (SCanning Imaging SpectroMeter for Atmopsheric CHartographY) by von Savigny and Lednyts'kyy (2013). In addition, a semi-annual oscillation was also reported from HRDI observations (Yee et al., 1997) and ISIS-2 observations (Cogger et al., 1981) of the O($^1$S) green line. Because the vertically integrated O concentration should be proportional to the integrated OH VER (see Eq.(2) in Mlynczak et al. (2013)), the same observed seasonal variability could also apply for the vertical OH($\nu$) shifts.

Based on the initial hypothesis that the collisional quenching with atomic oxygen is affecting the relative vertical OH($\nu$) shifts, we would therefore expect a coherent response in these shifts with the temporal evolution of the diurnal migrating tide. Accordingly, we focus on the seasonal and diurnal changes in the collisional quenching of OH with atomic oxygen. In addition, we will also consider the impact of collisional quenching with molecular oxygen, the second most efficient OH quencher after atomic oxygen (Adler-Golden, 1997). The advantage of our model approach is that we can deactivate the individual collisional quenching processes to study the associated impact on the relative vertical OH($\nu$) shifts. We compare these simulations with limb radiance observations from the SABER (Sounding of the Atmosphere by Broadband Emission Radiometry) instrument onboard of the TIMED (Thermosphere Ionosphere Mesosphere Energetics Dynamics) satellite and discuss the observed temporal variability of the vertical OH($\nu$) shifts with regard to our model results.

This paper is structured as follows. Section 2 introduces our OH quenching model and gives a brief summary on the SD-WACCM4 and SABER data. The methodology of our analysis on the relative vertical OH($\nu$) shifts is explained in Sect. 3. This is followed by a discussion on potential sources of error in Sect. 4. Based on a case example we reexamine important systematic features of the temporal variability of the OH emission layer and O quenching species in Sect.5 to establish an expectation on the temporal evolution of vertical OH($\nu$) shifts. In Sect. 6 we investigate the initial hypothesis on the role of collisional quenching on the vertical OH($\nu$) shifts by simulating the seasonal variability of the OH emission layer from the SD-WACCM4 data for different model assumptions. These simulations are then compared with experimental observations from SABER. Based on the same methods, the diurnal variability of the OH quenching process is investigated in

Sect. 7. We provide a summary of our results for the seasonal and diurnal variability of the relative vertical OH($\nu$) shifts in Sect. 8 and discuss their implications on the initial hypothesis.

## 2 Model and data description

### 2.1 Hydroxyl quenching model

A detailed description of the quenching model, which we use as a basis for our OH simulations, is given in McDade and Llewellyn (1988) and McDade (1991). Here, we limit our discussion to its primary key aspects and our adjustments to simulate absolute number densities of OH($\nu$).

As mentioned in the beginning, the Bates–Nicolet mechanism suggests the principal excitation mechanism of vibrationally excited OH according to the following reaction:

$$\mathrm{H} + \mathrm{O_3} \rightarrow \mathrm{OH}(\nu' \leq 9) + \mathrm{O_2} \qquad k_1 \text{(R1)}$$

where $k_1$ denotes the rate constant of this reaction. The released exothermic energy of this reaction leads to a preferred vibrational excitation between $\nu = 6$ and $\nu = 9$. In accordance with von Savigny et al. (2012) we assume the following processes to populate lower vibrational states:

- radiative cascade from the initially populated higher levels

  $$\mathrm{OH}(\nu') \rightarrow \mathrm{OH}(\nu'') + h\nu \qquad A(\nu', \nu'') \quad \text{(R2)}$$

- collisional relaxation

  $$\mathrm{OH}(\nu') + \mathrm{Q} \rightarrow \mathrm{OH}(\nu'') + \mathrm{Q} \qquad k_3^{\mathrm{Q}}(\nu', \nu'') \quad \text{(R3)}$$

  with Q = $\mathrm{O_2}$, $\mathrm{N_2}$.

- complete OH removal

  $$\mathrm{OH}(\nu') + \mathrm{Q} \rightarrow \text{other products} \qquad k_4^{\mathrm{Q}}(\nu', \nu'') \quad \text{(R4)}$$

  with Q = O, $\mathrm{O_2}$, $\mathrm{N_2}$.

Apart from these processes, the recombination of the perhydroxyl radical ($\mathrm{HO_2}$) with atomic oxygen as being proposed by Krassovsky (1963) could provide another mechanism to form OH with vibrational excitations below $\nu \leq 6$ at the mesopause. Different opinions exist on the importance of this mechanism to the general OH formation (e.g. see Khomich et al., 2008, for a summary of different studies), though the recent study by Xu et al. (2012) implicates that its contribution is rather negligible for vibrational states above $\nu = 3$. As we will discuss later, the main emphasis of our study is on vibrational states above $\nu = 3$, accordingly we neglect this mechanism in our following considerations.

Following McDade (1991), Eq. (3) in von Savigny et al. (2012) describes the OH concentration for steady state conditions. Here, we adjust this expression as follows:

$$[\mathrm{OH}(\nu)] = \left( A(\nu) + \sum_{\mathrm{Q}} k_L^{\mathrm{Q}}(\nu)[\mathrm{Q}] \right)^{-1} \times \left( P(\nu)\{k_1[\mathrm{H}][\mathrm{O_3}]\} + \sum_{\nu^*=\nu+1}^{9} [\mathrm{OH}(\nu^*)]\{A(\nu^*,\nu) + \sum_{\mathrm{Q}} k_3^{\mathrm{Q}}(\nu^*,\nu)[\mathrm{Q}]\} \right) \quad (1)$$

where $P$ is the nascent vibrational level distribution, $A(\nu)$ corresponds to the inverse radiative lifetime of OH and $k_L^{\mathrm{Q}}$ is the total rate constant for removal of OH in vibrational level $\nu$ through Reactions R3 and R4. Accordingly, we substitute the nascent production rate $p$ in von Savigny et al. (2012) by the $P(\nu)\{k_1[\mathrm{H}[\mathrm{O_3}]\}$ rate term in the nominator of Eq. (1). In contrast to the work of von Savigny et al. (2012), we do not normalise Eq. (1) with respect to the $\nu = 9$ vibrational state,because we aim to calculate absolute number densities of OH($\nu$) to allow for a direct comparison with the observed VER by SABER. Therefore, we have to implement absolute rate constants as well as absolute inverse radiative lifetimes in Eq. (1).

For our present model simulations we use the constants listed in Table 1, assuming that multiquantum relaxation only applies for quenching with $\mathrm{O_2}$, while the less efficient $\mathrm{N_2}$ quenching is limited to single-quantum relaxation only. If we apply these assumptions to Eq. (1), we get the following expression for OH as a function of vibrational state:

$$[\mathrm{OH}(\nu)] = \left( A(\nu) + k_L^{\mathrm{O_2}}(\nu)[\mathrm{O_2}] + k_L^{\mathrm{N_2}}(\nu)[\mathrm{N_2}] + k_L^{\mathrm{O}}(\nu)[\mathrm{O}] \right)^{-1} \times \left( P(\nu)\{k_1[\mathrm{H}][\mathrm{O_3}]\} + \sum_{\nu^*=\nu+1}^{9} [\mathrm{OH}(\nu^*)]\{A(\nu^*,\nu) + k_3^{\mathrm{O_2}}(\nu^*,\nu)[\mathrm{O_2}] + k_3^{\mathrm{N_2}}(\nu^*,\nu)[\mathrm{N_2}]\} \right) \quad (2)$$

with $k_3^{\mathrm{N_2}}(\nu^*,\nu) = 0$ for all $\{\nu^* > \nu + 1\}$ and $k_3^{\mathrm{N_2}}(\nu^*,\nu) = k_L^{\mathrm{N_2}}(\nu^*)$ for $\{\nu^* = \nu + 1\}$.

### 2.2 SD-WACCM4

The SD-WACCM4 simulations are based on the Whole Atmosphere Community Model, version 4 (WACCM4), which is a comprehensive free running chemistry-climate model. This model version is based on an earlier version described by Garcia et al. (2007) and has been recently extended, such that it is nudged to meteorological fields that are taken from the Global Earth Observing System Model, Version 5 (GEOS-5) of NASA's Global Modeling and Assimilation Office (GMAO).

SD-WACCM4 data were provided to us by courtesy of R. R. Garcia and D. E. Kinnison, NCAR Boulder. The same SD-WACCM4 simulations, which we consider in our study, were already applied to another study by Hoffmann et al. (2012) that investigates the dynamics of the model using mesospheric CO VMR measurements. We therefore refer to this paper for a more detailed description of the model. Here, we limit our discussion to the most relevant aspects to our study.

The nudging of SD-WACCM4 with GEOS-5 meteorological fields $\mathrm{M_{GEOS}}$ is performed up to 50 km altitude for each time step $t$ by replacing the model-predicted fields $\mathrm{M_{pred}}$ according to:

$$\mathrm{M_{pred}}(t) = 0.99 \cdot \mathrm{M_{pred}}(t) + 0.01 \cdot \mathrm{M_{GEOS}}(t).$$

Between 50 km and 60 km altitude a linearly decreasing relaxation scheme follows until it completely switches to a free-running mode above 60 km.

Despite the weak constraint of SD-WACCM4 by its relaxation to external meteorological fields from GEOS-5, Hoffmann et al. (2012) show that the upper (free-running) part is still strongly driven by the described nudging and closely reflecting the dynamic response, which they deduce from CO based measurements.

The horizontal resolution of the SD-WACCM4 data is $1.9° \times 2.5°$ in latitude and longitude. Its vertical extent reaches from the ground up to the lower thermosphere at about 137 km geopotential height (GPH) and it is divided into 66 height levels. The provided GPH values are transformed to geometric heights for our analysis. In the region from 80 km up to 95 km, which encloses the hydroxyl emission, the vertical distance between the model grid points varies from about 1.2 km to 3.6 km. The SD-WACCM4 simulations are initially performed at 0.5 h time increments, however, to save computational resources, global model results are stored as daily increments at 00:00 UTC. This limitation of our dataset prevents us from studying the diurnal evolution of the OH vertical profiles at a fixed geolocation. To overcome this constraint we make the assumption that the diurnal evolution of the vertical profiles is already contained within the zonal variation of each daily model result, i.e. we convert the longitudinal information to the Local Solar Time (LST). However, as we will discuss in Sect. 7.2, other processes exist, which can still complicate a direct comparison of the diurnal variability between SD-WACCM4 and SABER.

To simulate OH($\nu$) profiles by means of Eq. (2), we convert the SD-WACCM4 chemical profiles from VMR to absolute number densities based on the provided pressure and temperature fields. In addition, we consider the SD-WACCM4 temperatures for the calculation of the temperature dependent rate constant $k_1$ of reaction R1. The SD-WACCM4 data in this study cover the period between April 2010 and June 2011.

### 2.3 SABER

SABER is a multichannel infrared radiometer onboard of the TIMED satellite. Limb profiles are taken from a circular orbit at 625 km inclined at 74° to the equator and cover a latitudinal range from 54° S to 82° N or 82° S to 54° N, depending on the phase of the yaw cycle (Russell III et al., 1999). One yaw cycle of SABER corresponds to 60 days, i.e. due to the full precession of the instrument during one cycle, this period is required to get a full coverage of local times.

SABER is equipped with two channels sensitive to OH emissions, i.e. the 1.6 $\mu$m channel covers

emissions from the OH(5-3)/OH(4-2) transitions and the $2.0\mu\mathrm{m}$ channel covers emissions from the OH(9-7)/OH(8-6) transitions.

VER profiles from both channels are contained in the SABER Level 2a data products and will be used in our study. According to Mertens et al. (2009) the vertical resolution of the SABER VER profiles is approximately 2 km. Because the atmosphere is optically thin at altitudes above 80 km for wavelengths between $0.35$ and $2.0\mu\mathrm{m}$ (Khomich et al., 2008), the effect of self-absorption is negligible for the observed OH emission. Given this assumption, we can directly compare changes in our simulated OH concentrations to changes in the vertical VER profiles observed from both SABER channels.

In addition to measurements of the OH radiance, the latest SABER V2.0 data contain atomic oxygen profiles, which we use to study the impact of O quenching on the observed vertical shifts between the $1.6\mu\mathrm{m}$ and $2.0\mu\mathrm{m}$ VER profiles. As explained in Mlynczak et al. (2013), the SABER O concentrations are indirectly determined from the measured $2.0\mu\mathrm{m}$ VER profiles based on the steady state assumption:

$$\underbrace{k_1[\mathrm{H}][\mathrm{O_3}]}_{\propto \mathrm{VER}(2.0\mu\mathrm{m})} = k_2[\mathrm{O}][\mathrm{O_2}] \tag{R5}$$

with $k_2$ denoting the reaction rate constant between O and $O_2$ and $k_1[\mathrm{H}][\mathrm{O_3}]$ being directly proportional to the observed VER. At first glance, this seems to introduce a circular reasoning in our attempt to correlate O concentrations with the vertical shifts between the $1.6\mu\mathrm{m}$ and $2.0\mu\mathrm{m}$ VER profiles. This could potentially introduce a spurious (i.e. non-physical) correlation between both quantities, if the SABER model did not properly consider the real photochemistry and gaseous kinetics based on R5. However, Mlynczak et al. (2013) find a close agreement between their derived day- and nighttime O concentrations, which both rely on completely different methods. This indicates that the SABER model is reproducing physically meaningful O profiles. In turn, this should justify a direct comparison between SABER O concentrations and vertical shifts between both VER profiles, because we may suppose that any correlation between both quantities represents a real dependency between them.

## 3 Methodology

For the first part of this study we have to address some general features of the vertical OH profiles to provide a basis for our analysis on the collisional quenching process. Figure 1 shows vertical OH($\nu$) profiles that were simulated according to nighttime conditions at equatorial latitudes based on our model approach. In general, we will limit our discussion on the nighttime OH, because the relatively low abundances of daytime OH and the large Rayleigh scattering background makes a comparison with OH daytime observations more difficult.

In accordance with von Savigny et al. (2012) the vertical distribution of nighttime OH($\nu$) follows

single peak profiles that are shifted upwards with respect to their vibrational state. If we normalise each OH($\nu$) profile, the relative vertical shifts become clearly visible. In addition, we can notice a more pronounced vertical separation above the OH($\nu$) peak altitudes, which according to von Savigny et al. (2012) is related to the steep vertical gradient in O concentrations and the associated more pronounced collisional deactivation of OH at the upper part of the OH emission layer. By comparison, the vertical shifts between the OH($\nu$) profiles are significantly less pronounced below the profile peak altitudes.

The systematic increase of the vertical OH($\nu$) shifts above the profile peak altitudes seems to favour this altitude region for our study on the collisional quenching with O. However, it is important to keep in mind that any changes in the vertical OH($\nu$) shifts are the convolved response to changes in the quenching and source species concentrations Eq. (2). Therefore, finding the optimum reference points to compare the vertical shifts between two layers turns out to be less obvious than initially thought.

Another difficulty arises for the determination of relative peak shifts from the rather coarse vertical resolution of our simulated OH profiles and observed SABER VER profiles. Despite this constraint on the vertical resolution, we can benefit from the significantly higher dynamic range of the calculated number densities and observed VERs.

To quantify the vertical OH($\nu$) shifts at the peak altitudes and above, we therefore define two different reference points, which we determine for each vertical OH($\nu$) profile:

### D.1 weighted peak altitude: $Zpk_{\mathbf{weighted}}$

In analogy with von Savigny and Lednyts'kyy (2013) we weight the altitudes with the number density profile $N_{\mathrm{OH}}(\nu, z)$ for each OH($\nu$) layer:

$$Zpk_{\mathrm{weighted}}(\nu) = \frac{\int_0^\infty N_{\mathrm{OH}}(\nu, z')z'\mathrm{d}z'}{\int_0^\infty N_{\mathrm{OH}}(\nu, z')\mathrm{d}z'}$$

### D.2 shifted peak altitude: $Zpk_{\mathbf{+HWHM}}$

To sense changes between the vertical OH($\nu$) shifts in the upper part of the OH layer, we interpolate the altitude above the profile peak of each OH($\nu$) layer, where $N_{\mathrm{OH}}(\nu, z)$ has dropped by a factor of 0.5, i.e. the position that is shifted by the Half Width at Half Maximum (HWHM) above the profile peak.

For the SABER VER profiles, we can simply replace the number densities by the VERs in the above definitions.

## 4 Sources of error

While the inclusion of number densities according to D.1 and D.2 helps us to improve the vertical sensitivity of our model study, systematic departures between simulated and real number densities are a source of error for our investigation of the collisional quenching effects. The recently published study by Smith et al. (2013) indicates that WACCM tends to underestimate mesospheric ozone concentrations, which in turn will impact reaction R1. In addition, WACCM tends to overestimate mesospheric temperatures according to Smith (2012), which will affect our calculation of the rate constant $k_1$ and absolute number densities from the SD-WACCM4 temperature pressure fields.

Inspection of Eq. (2) shows that at least a linear departure in the H + $O_3$ source profiles from reality is not critical for our analysis, because they will cancel out in the calculation of the OH($\nu$) layer altitudes according to the above stated definitions. The situation is different for the quencher profiles, because any linear scaling of their concentrations cannot be completely factored out in Eq. (2). An overestimation of temperatures should in principle lead to an underestimation of the absolute quenching gas concentrations based on the ideal gas law. In contrast, too high temperatures will lead to an overestimation of the temperature dependent rate constant $k_1$. To get an estimate of the associated impact on the vertical shifts between different OH($\nu$) layers, we applied a constant offset of $-20$ K to our SD-WACCM4 temperatures. Based on this approach, the impact appears to be minor, i.e. in the order of a few tens of meters with regard to our later analysis of profile shifts based on D.1. With respect to the O quenching species the simulated concentrations tend to be lower compared to concentrations derived from SABER as shown in Smith et al. (2011). According to the initial hypothesis on the impact of the collisional quenching with O on the vertical shifts between different OH($\nu$) layers, an underestimated rate of collisional quenching should result in less pronounced vertical shifts. Apart from the discrepancies in simulated O concentrations, the uncertainty of its collisional rate constant $k_L^O$ will also affect our results. By comparison with the other quenchers, $k_L^O$ has the greatest uncertainty. If we apply the upper and lower boundary of the uncertainty estimates of $k_L^O$ from Xu et al. (2012), the changes to the vertical OH($\nu$) shifts based on D.1 range between about 100 m and 160 m with regard to our later analysis.

## 5 Simulated tidal signatures in OH and O: A monthly case example

Before we will address the temporal variability of vertical OH($\nu$) shifts, we have to reexamine systematic temporal changes of the entire OH emission layer and the O, $O_2$ quenching species for two reasons: First, we have to make sure that the temporal variability in the SD-WACCM4 data leads to a consistent evolution of the OH and O, $O_2$ species compared to previous studies. Second, this reexamination helps us to establish an expectation about the impact of temporal changes in the collisional quenching on the vertical OH($\nu$) shifts.

As motivated in the beginning, we will now consider a monthly case example around the Septem-

ber 2010 equinox, where the amplitude of the diurnal migrating tide maximises. For this month, a series of different model results is presented in Fig. 2. The global distribution of the integrated total column of all OH($\nu = 1, 2, .., 9$) layers is displayed for 00:00 (UTC) in Panel (a). A general eastward decrease in the integrated OH concentrations is clearly visible. In terms of LSTs, this corresponds to a decrease of integrated OH concentrations over the course of the night. In addition, the OH concentrations are generally high at equatorial latitudes and minimise around $\pm 30^\circ$ latitude, which is consistent with the study of Marsh et al. (2006) and other observational studies stated therein. The steep decrease of integrated OH concentrations at the outer latitudinal and longitudinal margins marks the terminator between day- and nighttime conditions.

Weighted OH peak altitudes $Zpk_{\text{weighted}}$ according to our previous definition D.1 are displayed in Panel (b). A systematic nighttime increase in the weighted OH peak altitudes by up to $4\,\mathrm{km}$ is again clearly visible. Accordingly, we find a significant anti-correlation between OH peak altitudes and concentrations in comparison with Panel (a). Indeed, previous studies based on observations made with the high-resolution Doppler imager (HRDI) instrument and the Wind Imaging Interferometer (WINDII) instrument onboard the upper atmosphere research satellite (UARS) revealed the same coherent anti-correlation between OH peak altitudes and integrated concentrations. Following Liu and Shepherd (2006) and the stated referenced therein, this anti-correlation may be associated to the vertical motions associated with tides or other processes (see also Cho and Shepherd (2006)).

As with the determination of OH($\nu$) profile peak altitudes, several possibilities exist to quantify temporal changes in the quenching species concentrations. The simplest method is to look at the diurnal evolution of a quenching species at a constant height level. However, this method neglects any changes of the quenching species concentrations that arise from the vertical motion of the entire OH layer. To account for this, we may determine the quenching species concentration at a fixed reference point of the OH layer. Again, this method is still rather simple, because the collisional quenching is not constrained to a fixed point at the OH layer. Thus, a more sophisticated approach is to quantify the collisional quenching by weighting the vertical quencher profiles with the corresponding OH profiles (i.e. replace $z'$ in D.1 with the number density $N_{\mathrm{Q}}(z')$ of the quenching species).

For our monthly case example, we applied the latter approach for the O concentrations in Panel (c) of Fig. 2. Accordingly, the equatorial weighted O concentrations show a pronounced maximum before midnight, which has also been confirmed by other observational studies (e.g. see Smith et al. (2010)) and should therefore lead to a pronounced collisional quenching of the OH emission layer at those LSTs. Furthermore, Smith et al. (2010) report another wavenumber 1 type feature at $\pm 30^\circ$ with opposite phase, which at least seems to be reflected at $30^\circ$S in our simulations. Of course, we have to bear in mind that we are considering a single month only and that the temporal variability of the OH emission layer is also affecting our weighted O concentrations. Moreover, following the study of Lu et al. (2012) the magnitude of the tidal amplitude seems to be slightly underestimated by WACCM4. Despite this slight underestimation, the tidal signatures in the OH profile weighted

O as well as the OH concentrations of our monthly case example show consistent characteristics with previous observations and should therefore serve as a plausible testing ground for the initial hypothesis on the collisional quenching.

If we expand our monthly case example to a full seasonal cycle, we would expect a semi-annual oscillation in the atomic oxygen concentrations, which are following the temporal changes in the amplitude of the diurnal-migrating tide as discussed before. Indeed, this oscillation is clearly visible in the simulated O concentrations, as shown in the left panel of Fig. 3. For this figure we choose an LST bin between -1 and 0 $\mathrm{hrs}$ around equatorial latitudes. Each curve represents one of the above discussed methods to quantify the O concentrations, i.e. O determined at the 0.241 $\mathrm{Pa}$ pressure level (green line), O interpolated at the selected OH($\nu = 5$) and OH($\nu = 9$) weighted profile peak altitude according to our definition D.1 (blue lines), O interpolated at the HWHM shifted position above the profile peak (see definition D.2 and red lines), and O weighted with either the selected OH($\nu = 5$) or OH($\nu = 9$) profile (black lines). Because we are interested in the relative temporal changes in the quenching species, each curve is subtracted by its minimum value (see legend) to allow for a better intercomparison.

In addition to atomic oxygen, we include the seasonal variability of molecular oxygen in the right panel of Fig. 3. Interestingly, we can find another semi-annual oscillation in phase with the atomic oxygen species, if we consider the curves that do not refer to the fixed 0.241 $\mathrm{Pa}$ level. Despite the lower quenching efficiency of $\mathrm{O_2}$ compared to O, the higher absolute $\mathrm{O_2}$ abundances will at least partially compensate this. Because of the increasing $\mathrm{O_2}$ number density with decreasing altitude, the collisional deactivation of excited OH($\nu$) through $\mathrm{O_2}$ quenching will be most pronounced at the lower part of the OH emission layer. Vice versa, the O quenching is rapidly decreasing at the lower part of the OH emission layer due to the steep vertical gradient in O number densities, thus, $\mathrm{O_2}$ quenching is expected to be the dominant process of vibrational deactivation of OH at the bottom of the OH emission layer. This already seems to indicate an important role of the seasonality in the $\mathrm{O_2}$ quenching with regard to the temporal evolution of vertical OH($\nu$) shifts.

## 6 Seasonal evolution of OH layer shifts

### 6.1 Sensitivity study

In the following, we will compare relative changes in the vertical shifts between the OH($\nu = 9$) and OH($\nu = 5$) profiles. We select these two vibrational states because each of them contributes to emissions, which can be observed by either the 1.6 $\mu\mathrm{m}$ or 2.0 $\mu\mathrm{m}$ SABER channel. Ideally, one must consider that each SABER channel captures a mixture of emissions that belong to two different transition bands. However, because the difference in vibrational levels between each transmission is limited to $\Delta\nu = 1$, we assume that we can neglect the effect of profile mixing for each channel, if we are interested in the relative vertical shift between both (mixed) OH profiles. The vertical

shift between a simulated OH($\nu = 9$) and OH($\nu = 5$) profile will be calculated from the difference between either their weighted peak altitudes:

$$\Delta Zpk_{\text{weighted}} = Zpk_{\text{weighted}}[\text{OH}(\nu = 9)] - Zpk_{\text{weighted}}[\text{OH}(\nu = 5)], \tag{3}$$

or from the difference between the HWHM shifted altitudes above the profile peaks:

$$\Delta Zpk_{\text{+HWHM}} = Zpk_{\text{+HWHM}}[\text{OH}(\nu = 9)] - Zpk_{\text{+HWHM}}[\text{OH}(\nu = 5)]. \tag{4}$$

The vertical shifts between the SABER 1.6 $\mu$m and 2.0 $\mu$m VER profiles are determined in the same way.

We will now investigate the seasonal variability of the relative vertical shifts between our simulated OH($\nu = 9$) and OH($\nu = 5$) profiles, which we denote as OH(9;5) profile shifts in the following. For this task, we perform three different model runs:

- all quenching species are activated
- O quenching species is deactivated
- $O_2$ quenching species is deactivated

This allows us to study the impact of collisional quenching on the OH(9;5) profile shifts for both species.

The results from our three model runs are shown in Fig. 4. Panel (a) displays the seasonal evolution of OH(9;5) profile shifts for the first model run (i.e. complete quenching considered). The left axis/solid line refer to the relative vertical shifts between weighted peak altitudes according to Eq. (3). The right/dashed line refer to the relative vertical shifts at the upper part of the OH(9;5) layers according to Eq. (4). If we concentrate on the solid line first, we find indeed a semi-annual oscillation in the OH(9;5) profile shifts that is in phase with the observed changes in the O and $O_2$ concentrations according to Fig. 3. On the other hand, if we look at the upper part of the OH(9;5) layers (dashed line), the fluctuations in the seasonal variability are much more pronounced and the response to the seasonal changes in the quenching species is less clear. So far, we find the best agreement with the initial hypothesis on the collisional quenching process for our weighted peak altitude definition D.1.

Similar to Panel (a), Panel (b) shows the model run with the deactivated O quenching process. For both lines, we find a significant decrease in the OH(9;5) profile shifts, which again is consistent with the initial hypothesis. On the other hand, we still find a persisting semi-annual oscillation for the solid line (i.e. OH(9;5) profile shifts with respect to weighted peak altitudes) that is superimposed by another temporal maximum around mid January 2010. The seasonal response at the upper part of the OH(9;5) layers (dashed line) remains less clear. If we now subtract the results from the model runs with and without O quenching, we find a clear semi-annual response in the OH(9;5) profile shifts according to the solid line in Panel (c). Interestingly, if we compare the increase in the

OH(9;5) profile shifts between July and October between Panel (b) and (c), the contribution of the O quenching process to the temporal changes in the OH(9;5) profile shifts is just slightly above the remaining temporal changes for the model run with deactivated O quenching. With regard to the initial hypothesis, this suggests that we cannot address the observed seasonality in OH(9;5) profile shifts to the modulation in the collisional O quenching only.

We therefore repeat the same investigation of the collisional quenching process for the $O_2$ quencher. In analogy with Panel (c), Panel (d) shows the difference in OH(9;5) profile shifts when subtracting the results from the model runs with activated and deactivated $O_2$ quenching. Again, the upper part of the OH(9;5) layers shows strong fluctuations (dashed lines), thus we will limited our discussion to the relative shifts between weighted peak altitudes (solid line). First of all, we find that the deactivation of the $O_2$ quenching in our model run leads to a still noticeable decrease in the vertical OH(9;5) profile shifts. If we neglect the maximum around January 2011, we can find a further semi-annual response in the vertical OH(9;5) profile shifts due to the switching between the deactivated and activated $O_2$ quenching. In comparison with the seasonal change in the OH(9;5) profile shifts between July and October due to the deactivation of the O quenching (see panel c), the impact of the deactivation of $O_2$ quenching is less than one half.

With respect to the model run that considers all quenching species (see Panel a), we notice that simply adding the effect of O and $O_2$ quenching according to Panel (c,d) still leads to considerably smaller vertical OH(9;5) profile shifts, as shown in Panel (d). On the other hand, the agreement in the seasonal variability between Panel (a) and (d) is quite good. This becomes evident, if we determine the best scaling factor between both functions in a least-squares sense. Accordingly, the grey line in Panel (d) denotes the $\Delta Zpk_{\text{weighted}}$ profile shift values from Panel (a) divided by 1.438. Apparently, taking the sum of Panel (c,d) leads to an improved agreement in the seasonal variability with respect to Panel (a) rather than considering the effect of deactivating either O or $O_2$ quenching only. This again suggests the importance of the $O_2$ quenching to the seasonal variability. Still, the question remains, why the sum of Panel (c,d) is smaller by a factor of 1.438 compared to the complete quenching model run in Panel (a). As noticed before, the impact of $N_2$ quenching is insufficient to serve as an explanation, i.e. it leads to a difference between 40 $\mathrm{m}$ to 50 $\mathrm{m}$, if we subtract a model run with deactivated $N_2$ quenching from the complete quenching case in Panel (a) (not shown). This indicates that the combined effect of O and $O_2$ quenching is larger than the sum of their individual contributions.

As discussed in the beginning, seasonal changes in the vertical H+$O_3$ profiles will affect the OH emission layer width, which in turn will also affect the OH(9;5) profile shifts. In addition to the combined effect of O and $O_2$ quenching, this could provide another mechanism that is driving the temporal variability. The seasonal evolution of the OH emission layer width is shown in Panel (f) of Fig. 4. In this case, we determine the width of the vertical profile by the Full Width at Half Maximum (FWHM) to account for changes above and below the profile peak altitude. Accordingly, we find

a pronounced increase around the mid of January 2011 in the FWHM values, which is coherent with the observed additional increase in the OH(9;5) profile shifts for the deactivated O quenching case (Panel b). This gives an explanation, why the drop in the vertical OH(9;5) profile shifts is less pronounced after the winter solstice according to Panel (a). Furthermore, the larger extent of the OH profile width may also favour the rate of collisional $O_2$ quenching, which could explain the coherent response according to Panel (d) of Fig. 4. On the other hand, a coherent semi-annual variability with respect to the $\Delta Zpk_{\text{weighted}}$ profile shift values in Panel (a) is not evident, which strengthens the argument of the combined effect of O and $O_2$ quenching as the dominant driving mechanism of the seasonal variability in the OH(9;5) profile shifts.

Finally, we also consider the relative changes of the OH(9) and OH(5) peak widths, which should particularly influence the OH(9;5) profile shifts above the profile peak altitudes. The seasonal evolution of each peak width is shown by the grey lines in Panel (g) of Fig. 4 (see caption). The difference we receive by subtracting both temporal evolutions with each other is shown by the black solid line. We find that the large relative changes in the profile widths around October 2010 and May 2011 are coherent with the observed jumps in the OH(9;5) profile shifts at the upper part of the OH(9;5) layers (see dashed line in Fig. 4a), i.e. the vertical shifts $\Delta Zpk_{\text{+HWHM}}$ appear to react more sensitively to relative changes in the OH(9;5) profile widths.

### 6.2 Comparison with SABER

We will now focus on the seasonal variability of the vertical shifts between the SABER 1.6 and 2.0 µm VER profiles for the period from January 2009 to December 2011. In analogy with our sensitivity study, we choose the same $-1$ h to 0 h LST bin for the results presented in Fig. 5. Here, each point represents the mean value based on three matching yaw-cycles between 2009 to 2011. Each error bar denotes the corresponding standard deviation. Panel (a-b) show the seasonal variability in the VER profile shifts for two equatorial latitude bins. Again, the solid line refers to the vertical shifts between weighted peak altitudes according to Eq. 3 (left axis) and the dashed line refers to the vertical shifts at the upper part of the VER profiles according to Eq. 3 (right axis). The seasonal variability of derived O concentrations is displayed in Panel (c-d). The black line shows the O concentrations at 90 km altitude (left axis). The grey dotted and dashed lines show the VER profile weighted O concentrations with respect to the 1.6 µm and 2.0 µm channel (right axis). Panel (e-f) show the seasonal variability of the 1.6 and 2.0 µm VER profile widths (dashed and dotted, left axis) as well as their relative difference (black solid line, right axis).

First of all, we notice that a semi-annual oscillation - with maxima around May and October - is also present in the SABER VER profile shifts. Indeed, we find another coherent semi-annual oscillation in the O concentrations for the $0°$ to $10°$ S bin. With regard to the $0°$ to $10°$ N bin a faint semi-annual structure is present, but the overall change is dominated by an annual oscillation. Interestingly, in comparison with the changes in the SABER VER profile shifts, the semi-annual

response is more dominating in the $10^\circ$ N rather than the $10^\circ$ S latitude bin. Again, this indicates that the consideration of O quenching alone cannot sufficiently explain the seasonal variability of SABER VER profile shifts. In contrast to our model results, we cannot directly rule out that changes in the sources gases may significantly affect the seasonality of the observed VER profile shifts, because of the limited spectral bandwith of SABER, which prevents us from sensing all Meinel bands of the OH emission.

If we consider the relative changes of the VER profile widths according to the black solid line in Panel (e-f) of Fig. 5, we can find a similar coherent response in the vertical shifts at the upper part of both VER profiles (see dashed line in panel a-b), which again shows the stronger sensitivity of this profile shift definition to changes in the relative profile shapes.

## 7 Diurnal evolution of OH layer shifts

### 7.1 Sensitivity study

In analogy with our analysis of the seasonal variability of the vertical OH(9;5) profile shifts in the previous section, we perform the same three model runs where we consider the full-quenching case, the deactivation of O quenching and the deactivation of $O_2$ quenching. To improve our later comparison with the observed diurnal variability from SABER, we adjust the temporal averaging period in our model runs to the same period that is required for a full SABER yaw cycle.

Accordingly, Fig. 6 shows the diurnal variability of both simulated quenching species around the September 2010 equinox at equatorial latitudes, where the amplitude of the diurnal migrating tide maximises. Again, we use the same definitions to quantify changes in the O and $O_2$ concentrations as in Fig. 3.

While the different definitions of O concentrations only lead to a slight phase shift in the temporal evolution of the O concentrations of up to one hour, the different definitions of $O_2$ concentrations can result in quite different diurnal evolutions. With regard to the systematic increase in the nighttime OH peak altitudes (Fig. 2b), the decrease in the OH profile weighted $O_2$ concentrations (black lines) and interpolated $O_2$ concentrations at the weighted OH peak altitude (blue lines) appears to be the most consistent.

The results from our three model runs are shown in Fig. 7, with the solid lines (left axis) referring to the OH(9;5) profile shift according to Eq. (3) and the dashed lines (right axis) referring to Eq. (4) correspondingly. Panel (a) displays the peak shifts for the first model run, which considers all quenching species. Panel (b) shows the OH(9;5) profile shifts for the model run with deactivated O quenching. Panel(c-d) show the difference in OH(9;5) profile shifts, if we subtract either the model run with deactivated O or $O_2$ quenching from the full quenching model run shown in Panel (a). Similar to the previous section, we also include the sum of Panel (c,d) in Panel (e).

Keeping in mind the initial hypothesis on the effect of collisional quenching, we would expect

that the vertical OH(9;5) profile shifts should maximise shortly before midnight according to the maximising O concentrations. However, neither of both OH(9;5) profile shift definitions matches with this expectation according to Panel (a). Furthermore, we notice that the diurnal variability in the OH(9;5) profile shift is rather opposite for both definitions. If we switch off the O quenching according to our second model run (Panel b), the vertical OH(9;5) profile shifts are significantly reduced as it was also the case for our investigation of the seasonal variability in Fig. 4b. Moreover, if we consider the impact of the collisional O quenching according to Panel (c), a coherent response to the diurnal evolution of O is clearly visible for the $\Delta Zpk_{\text{weighted}}$ values (solid line). For the HWHM shifted positions above the profile peaks (dashed line), we can still find a significant internal variability, such that the impact of collisional O quenching again remains less clear.

As with our analyis of the seasonal variability, the collisional $O_2$ quenching is also significantly affecting the vertical OH(9;5) profile shifts according to Panel (d) of Fig. 7. In comparison with the collisional O quenching the effect is still smaller with regard to the weighted peak altitudes. Furthermore, the relative changes due to the deactivation of $O_2$ quenching remain rather constant after $-2$ hrs. In contrast, if we consider the results based on the HWHM shifted locations, the effect of the deactivation of $O_2$ quenching strongly exceeds the corresponding effect for O. Moreover, the early $Zpk_{\text{weighted}}[\text{OH}(5)]$ positions are even higher than those of the $Zpk_{\text{weighted}}[\text{OH}(9)]$ positions, which leads to the negative values before $-3$ hrs.

If we consider the sum of Panel (c,d), as shown in Panel (e), the resulting OH(9;5) profile shifts are again significantly smaller compared to the model run in Panel (a) which considers all quenching species simultaneously. Interestingly, if we search for the best scaling factor between both panels, we obtain a factor of 1.430, which is very close to the scaling factor we receive for the seasonal variability. On the other hand, the agreement between the diurnal evolution according to the sum of Panel (c,d) and the scaled Panel (a), which is denoted by the grey line in Panel (e), is less clear for the early evening hours. During the same hours, we notice a strong shrinking of the entire OH emission layer by up to 4 km due to the nighttime evolution of the H+$O_3$ source gases according to Fig. 8a. This may also provide an explanation for the departure between the sum of Panel (c,d) and scaled Panel (a), presuming that the combined effect of O and $O_2$ quenching can be described by its linearly scaled sum according to Fig. 7. With regard to the OH(9;5) profile shifts based on $\Delta Zpk_{+\text{HWHM}}$ values (dashed lines), we find that these are again strongly correlated with the relative changes in the OH(9,5) profile widths according to Fig. 8b.

We expand our analysis to the full year of simulated OH($\nu$) populations and summarise the found correlations between vertical OH(9;5) profile shifts and quenching species concentrations in Fig. 9 and Fig. 10. Following the displayed correlation plots in Fig. 9, we find no significant correlation between the vertical OH(9;5) profile shifts and weighted OH(9) concentrations for all seasons and both peak shift definitions. A weak positive correlation is only visible, if we include all data points in Panel (a). As with our equinoctial case example according to Fig. 7c, the correlation between vertical

OH(9;5) profile shifts and weighted O concentrations significantly improves, if we compare the relative changes between the model runs with activated and deactivated O quenching for weighted peak altitudes (Fig. 9c). In contrast, the correlation remains poor, if we consider OH(9;5) profile shifts at the upper part of both layers (Fig. 9d).

Figure 10 shows the corresponding correlations for the $O_2$ quencher. In contrast to the O quencher, the correlations with the vertical OH(9;5) profile shifts are exceptionally high. Of course we have to bear in mind that the systematic increase in the OH nighttime altitudes (see Fig. 2b) will also be reflected in the systematic decrease in OH(9) weighted $O_2$ concentrations. However, for the relative changes between the model runs with activated and deactivated $O_2$ quenching, we still find a significant correlation in Panel (c), respectively anti-correlation in Panel (d) of Fig. 10.

In summary, the nighttime evolution in the OH(9;5) profile shifts can hardly be explained by the process of collisional quenching with atomic oxygen only. Again, the inclusion of molecular oxygen quenching further improves the correlation with the OH(9;5) profile shifts. In addition, the simultaneous strong decrease of the entire OH layer width, driven by the $H+O_3$ source profiles, will further impact the nighttime evolution of OH(9;5) profile shifts. Interestingly, the systematic changes in OH peak altitudes and associated changes in $O_2$ concentrations show a very strong correlation with the temporal changes in the vertical OH(9;5) profile shifts.

### 7.2 Observed diurnal variability from SABER

For the SABER observations we first consider the same yaw-cycle that was also used for the model simulations presented in Fig. 7 and compare the relative shifts between the 1.6 $\mu m$ and 2.0 $\mu m$ VER profiles with the OH-VER weighted atomic oxygen profiles similar to our analysis on the seasonal variability. For the observed diurnal variability, it is important to note that the temporal evolution in the observed relative OH profile shifts may significantly differ from our model results because of the existence of additional non-migrating tides as being reported by Xu et al. (2010) from SABER observations at lower latitudes. These tides would complicate a direct comparison with our model results, since we have to extract the temporal evolution from the longitudinal variability of our 00:00 UTC model outputs. However, despite the possible existence of non-migrating tides, this does not prevent us from testing the hypothesis on the impact of collisional quenching with regard to the temporal variability of the O quenching species.

In analogy with Fig. 7 the SABER results are shown in Fig. 11 for the same yaw-cycle and for two latitudinal bins nearby the equator. Indeed, the nighttime evolution of relative OH profile shifts looks quite different compared to our modelled vertical OH(9,5) profile shifts. Furthermore, the amplification of atomic oxygen before midnight is not as evident as in our model results. Despite these discrepancies, we would expect from the systematic nighttime decrease in atomic oxygen a corresponding feedback in the vertical VER peak shifts, which clearly is not the case. Again, we also notice strong changes in the relative peak widths according to Panel (e) and (f) of Fig. 7 that are

partially reflected in the nighttime changes of VER peak shifts.

If we expand our analysis to a full seasonal cycle, the missing correlation between VER profile shifts and O concentrations remains. Accordingly, the process of collisional O quenching appears to be insufficient to explain the nighttime evolution of the OH VER profile shifts, which also agrees with our model expectations in a qualitative sense.

## 8 Summary and Conclusion

Following the hypothesis that the process of collisional quenching is significantly affecting the vertical shifts between different OH($\nu$) layers, this study investigated the impact of the temporal variability of the collisional quenching on the seasonal as well as the diurnal evolution of the vertical shifts between the OH(9) and OH(5) layer. This was done by establishing an updated quenching model, which uses the model output from a state-of-the-art 3D chemical climate model (SD-WACCM4) to simulate the temporal variability of both OH($\nu$) layers.

By comparing different model runs, which consider either all quenching species or neglect the collisional quenching process by O or $O_2$, we could study the actual impact of the temporal variability of O and $O_2$ quenching on the vertical OH(9;5) profile shifts. For the seasonal variability we find that both quenchers have a noticeable impact on the vertical OH(9;5) profile shifts, which manifests in a semi-annual variability that is following the temporal evolution of the diurnal migrating tide at the equator. Furthermore, the simultaneous quenching of both species results in about 1.4x larger vertical OH(9;5) profile shifts than we would receive from the sum of their individual contributions. With regard to previous studies that were mainly focusing on the effect of collisional quenching with O, this indicates the important role of the combined effects of O and $O_2$ quenching on the vertical structure of the OH layer. In addition, the strong change in the OH emission layer widths around January 2011 demonstrates that temporal changes in the H+$O_3$ profiles provide another mechanism to affect the OH(9;5) profile shifts.

We found further evidence of the same seasonality in the OH(9;5) profile shifts in the SABER observations, even though the coherence with changes in the derived SABER O concentrations is not always as clearly pronounced as it is the case in our model simulations. This could reflect the stronger temporal variability in the true H+$O_3$ profiles, which is competing with the temporal changes in the collisional quenching processes.

With regard to the diurnal variability our model study as well as our analysis of SABER VER profiles clearly show that the collisional quenching process of OH with O is insufficient to describe the temporal evolution alone. Again, the consideration of the combined effect of O and $O_2$ quenching is required to describe the temporal shifts in the OH(9;5) profiles. In addition, the model results suggest that the nighttime evolution of the H+$O_3$ profiles is significantly affecting the vertical OH(9;5) profile shifts for the first half of the night.

In summary, according to this study the effect of the collisional quenching does have a noticeable impact on the temporal variability of OH(9;5) profile shifts at the equator, but requires the simultaneous consideration of the O and $O_2$ quenching species to provide a proper description of the observed temporal evolution. While the O and $O_2$ quenching appears to be modulated in phase with regard to their seasonal evolution, the need of the simultaneous consideration of both quenching species becomes even more important for the diurnal evolution, where the modulation of O and $O_2$ can differ substantially, such that we cannot find a meaningful correlation to changes in the O quenching alone.

Critical assumptions of this study include:

- absolute number densities derived from SD-WACCM4 temperatures (too warm),
- simulated diurnal variability described by zonal variation of daily model output (conflicting with non-migrating tides),
- SABER O concentrations indirectly determined from OH Meinel emission.

Furthermore, the large uncertainty in the collisional quenching rate constant $k_L^O$ appears to have the most significant impact on our results, showing the need for improving our understanding in the collisional quenching process.

Because of the manifold of transition bands being observed by different ground-based instruments, a thorough understanding of the driving processes of the variability of OH emission altitudes is crucial for the intercomparison and interpretation of long-term data sets. This in particular applies for studying of mesopause temperature trends by means of OH rotational temperature measurements (see Beig et al. (2003); Beig (2011) for a comprehensive review on this topic). Further improvements in the modelling of the tidal variability at the mesopause as well as the inclusion of a multiyear analysis of the features that have been discussed here would further contribute to a better quantitative understanding of the systematic biases between different observational long-term studies.

*Acknowledgements.* This work was in part supported by Ernst-Moritz-Arndt-University of Greifswald. Further support was granted by the German Research Foundation (Deutsche Forschungsgemeinschaft, DFG) under project PA 1714/4-2. We thank R. R. Garcia and D. E. Kinnison, NCAR Boulder, for providing the SD-WACCM4 data to us, which have been a crucial component of this study. In addition, we thank C. Hoffman, former member of the IUP Bremen and A. K. Smith, NCAR Boulder, for the helpful discussions on the SD-WACCM4 data and the employed quenching model to this study. Finally, we are indebted to the SABER team for making SABER data available.

## References


Adler-Golden, S.: Kinetic parameters for OH nightglow modeling consistent with recent laboratory measurements, J. Geophys. Res., 102, 19 969–19 976, doi:10.1029/97JA01622, 1997.

Baker, D. J. and Stair Jr, A. T.: Rocket measurements of the altitude distributions of the hydroxyl airglow, Physica Scripta, 37, 611–, doi:10.1088/0031-8949/37/4/021, 1988.

Bates, D. R. and Nicolet, M.: The photochemistry of atmospheric water vapor, J. Geophys. Res., 55, 301–327, doi:10.1029/JZ055i003p00301, 1950.

Beig, G.: Long-term trends in the temperature of the mesosphere/lower thermosphere region: 2. Solar response, J. Geophys. Res., 116, A00H12–, doi:10.1029/2011JA016766, 2011.

Beig, G., Keckhut, P., Lowe, R. P., Roble, R. G., Mlynczak, M. G., Scheer, J., Fomichev, V. I., Offermann, D., French, W. J. R., Shepherd, M. G., Semenov, A. I., Remsberg, E. E., She, C. Y., Lübken, F. J., Bremer, J., Clemesha, B. R., Stegman, J., Sigernes, F., and Fadnavis, S.: Review of mesospheric temperature trends, Rev. Geophys., 41, 1015–, doi:10.1029/2002RG000121, 2003.

Cho, Y.-M. and Shepherd, G.: Correlation of airglow temperature and emission rate at Resolute Bay (74.86°N), over four winters (2001-2005), Geophys. Res. Lett., 33, L06 815–, doi:10.1029/2005GL025298, 2006.

Cogger, L. L., Elphinstone, R. D., and Murphree, J. S.: Temporal and latitudinal 5577 A airglow variations, Can. J. Phys., 59, 1296–1307, doi:10.1139/p81-170, 1981.

Dodd, J. A., Lipson, S. J., Lowell, J. R., Armstrong, P. S., Blumberg, W. A. M., Nadile, R. M., Adler-Golden, S. M., Marinelli, W. J., Holtzclaw, K. W., and Green, B. D.: Analysis of hydroxyl earthlimb airglow emissions: Kinetic model for state-to-state dynamics of OH ($\nu$,N), J. Geophys. Res., 99, 3559–3585, doi:10.1029/93JD03338, 1994.

Garcia, R. R., Marsh, D. R., Kinnison, D. E., Boville, B. A., and Sassi, F.: Simulation of secular trends in the middle atmosphere, 1950;2003, J. Geophys. Res., 112, D09 301–, doi:10.1029/2006JD007485, 2007.

Hoffmann, C. G., Kinnison, D. E., Garcia, R. R., Palm, M., Notholt, J., Raffalski, U., and Hochschild, G.: CO at 40-80 km above Kiruna observed by the ground-based microwave radiometer KIMRA and simulated by the Whole Atmosphere Community Climate Model, Atmos. Chem. Phys., 12, 3261–3271, doi:10.5194/acp-12-3261-2012, 2012.

Khomich, V., Semenov, A., and Shefov, N.: Airglow as an Indicator of Upper Atmospheric Structure and Dynamics, Springer Berlin Heidelberg, doi:10.1007/978-3-540-75833-4, 2008.

Krassovsky, V. I.: Chemistry of the upper atmosphere, Space Res., 3, 96–116, 1963.

Liu, G. and Shepherd, G. G.: An empirical model for the altitude of the OH nightglow emission, Geophys. Res. Lett., 33, L09 805–, doi:10.1029/2005GL025297, 2006.

Lu, X., Liu, H.-L. L., Liu, A. Z., Yue, J.M. McInerney, J. M., and Z, L.: Momentum budget of the migrating diurnal tide in the Whole Atmosphere Community Climate Model at vernal equinox, J. Geophys. Res., 117, D07 112, doi:10.1029/2011JD017089, 2012.

Makhlouf, U. B., Picard, R. H., and Winick, J. R.: Photochemical-dynamical modeling of the measured response of airglow to gravity waves 1. Basic model for OH airglow, J. Geophys. Res., 100, 11 289–11 311, doi:10.1029/94JD03327, 1995.

Marsh, D. R., Smith, A. K., Mlynczak, M. G., and Russell, J. M.: SABER observations of the OH Meinel airglow variability near the mesopause, J. Geophys. Res., 111, A10S05–, doi:10.1029/2005JA011451, 2006.

McDade, I. C.: The altitude dependence of the OH($X^2\Pi$) vibrational distribution in the nightglow: Some model expectations, Planetary and Space Science, 39, 1049–1057, doi:10.1016/0032-0633(91)90112-N, 1991.

McDade, I. C. and Llewellyn, E. J.: Mesospheric oxygen atom densities inferred from night-time OH Meinel band emission rates, Planetary and Space Science, 36, 897–905, doi:10.1016/0032-0633(88)90097-9, 1988.

Mertens, C. J., Russell III, J. M., Mlynczak, M. G., She, C.-Y., Schmidlin, F. J., Goldberg, R. A., López-Puertas, M., Wintersteiner, P. P., Picard, R. H., Winick, J. R., and Xu, X.: Kinetic temperature and carbon dioxide from broadband infrared limb emission measurements taken from the TIMED/SABER instrument, Adv. Space. Res., 43, 15–27, doi:10.1016/j.asr.2008.04.017, 2009.

Mlynczak, M. G., Hunt, L. A., Mast, J. C., Thomas Marshall, B., Russell, J. M., Smith, A. K., Siskind, D. E., Yee, J.-H., Mertens, C. J., Javier Martin-Torres, F., Earl Thompson, R., Drob, D. P., and Gordley, L. L.: Atomic oxygen in the mesosphere and lower thermosphere derived from SABER: Algorithm theoretical basis and measurement uncertainty, J. Geophys. Res. Atmos., 118, 5724–5735, doi:10.1002/jgrd.50401, 2013.

Rothman, L., Gordon, I., Barbe, A., Benner, D., Bernath, P., Birk, M., Boudon, V., Brown, L., Campargue, A., Champion, J.-P., Chance, K., Coudert, L., Dana, V., Devi, V., Fally, S., Flaud, J.-M., Gamache, R., Goldman, A., Jacquemart, D., Kleiner, I., Lacome, N., Lafferty, W., Mandin, J.-Y., Massie, S., Mikhailenko, S., Miller, C., Moazzen-Ahmadi, N., Naumenko, O., Nikitin, A., Orphal, J., Perevalov, V., Perrin, A., Predoi-Cross, A., Rinsland, C., Rotger, M., Šimečková, M., Smith, M., Sung, K., Tashkun, S., Tennyson, J., Toth, R., Vandaele, A., and Vander Auwera, J.: The HITRAN 2008 molecular spectroscopic database, JQSRT, 110, 533–572, doi:10.1016/j.jqsrt.2009.02.013, 2009.

Russell III, J. M., Mlynczak, M. G., Gordley, L. L., Tansock, Jr., J. J., and Esplin, R. W.: Overview of the SABER experiment and preliminary calibration results, in: Society of Photo-Optical Instrumentation Engineers (SPIE) Conference Series, edited by Larar, A. M., vol. 3756 of Society of Photo-Optical Instrumentation Engineers (SPIE) Conference Series, pp. 277–288, doi:10.1117/12.366382, 1999.

Sander, S. P., Abbatt, J., Barker, J. R., Burkholder, J. B., Friedl, R. R., Golden, D. M., Huie, R. E., Kolb, C. E., Kurylo, M. J., Moortgat, G. K., Orkin, V. L., and Wine, P. H.: Chemical Kinetics and Photochemical Data for Use in Atmospheric Studies, Evaluation No. 17, JPL Publication, Jet Propulsion Laboratory, Pasadena, 10-66, 1–12, 2011.

Shepherd, M. G., Liu, G., and Shepherd, G. G.: Mesospheric semiannual oscillation in temperature and nightglow emission, Journal of Atmospheric and Solar-Terrestrial Physics, 68, 379–389, doi:10.1016/j.jastp.2005.02.029, 2006.

Smith, A. K.: Global dynamics of the MLT, Surv Geophys, 33, 1177–1230–, doi:10.1007/s10712-012-9196-9, 2012.

Smith, A. K., Marsh, D. R., Mlynczak, M. G., and Mast, J. C.: Temporal variations of atomic oxygen in the upper mesosphere from SABER, J. Geophys. Res., 115, D18 309–, doi:10.1029/2009JD013434, 2010.

Smith, A. K., Garcia, R. R., Marsh, D. R., and Richter, J. H.: WACCM simulations of the mean circulation and trace species transport in the winter mesosphere, J. Geophys. Res., 116, D20 115–, doi:10.1029/2011JD016083, 2011.

Smith, A. K., Harvey, V. L., Mlynczak, M. G., Funke, B., García-Comas, M., Hervig, M., Kaufmann, M., Kyrölä, E., López-Puertas, M., McDade, I., Randall, C. E., Russell, J. M., Sheese, P. E., Shiotani, M., Skinner, W. R., Suzuki, M., and Walker, K. A.: Satellite observations of ozone in the upper mesosphere, J.

Geophys. Res. Atmos., 118, 5803–5821, doi:10.1002/jgrd.50445, 2013.

Steinfeld, J. I., Adler-Golden, S. M., and Gallagher, J. W.: Critical survey of data on the spectroscopy and kinetics of ozone in the mesosphere and thermosphere, Phys. Chem. Ref. Data, 16, 911–951, doi:10.1063/1.555796, 1987.

von Savigny, C. and Lednyts'kyy, O.: On the relationship between atomic oxygen and vertical shifts between OH Meinel bands originating from different vibrational levels., Geophys. Res. Lett., n/a, n/a–n/a, doi:10.1002/2013GL058017, 2013.

von Savigny, C., McDade, I. C., Eichmann, K.-U., and Burrows, J. P.: On the dependence of the OH* Meinel emission altitude on vibrational level: SCIAMACHY observations and model simulations, Atmos. Chem. Phys., 12, 8813–8828, doi:10.5194/acp-12-8813-2012, 2012.

Xu, J., Smith, A. K., Jiang, G., Gao, H., Wei, Y., Mlynczak, M. G., and Russell, J. M.: Strong longitudinal variations in the OH nightglow, Geophys. Res. Lett., 37, L21 801–, doi:10.1029/2010GL043972, 2010.

Xu, J., Gao, H., Smith, A. K., and Zhu, Y.: Using TIMED/SABER nightglow observations to investigate hydroxyl emission mechanisms in the mesopause region, J. Geophys. Res., 117, D02 301–, doi:10.1029/2010GL043972, 2012.

Yee, J.-H., Crowley, G., Roble, R. G., Skinner, W. R., Burrage, M. D., and Hays, P. B.: Global simulations and observations of O($^1$S), O$_2$($^1\Sigma$) and OH mesospheric nightglow emissions, J. Geophys. Res., 102, 19 949–19 968, doi:10.1029/96JA01833, 1997.

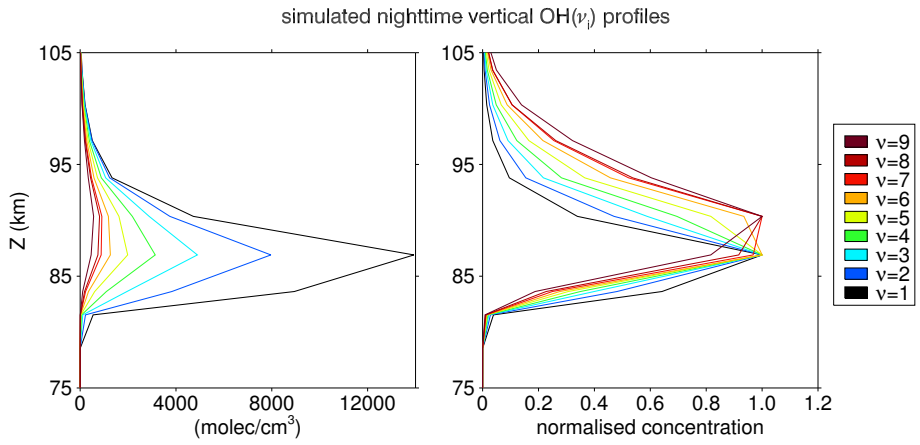


Fig. 1: Vertical OH($\nu$) profiles calculated from monthly averaged SD-WACCM4 model output for September 2010, 00:00 UTC at the 0° equatorial latitude. Left panel: absolute number concentrations. Right panel: normalised OH($\nu$) profiles.

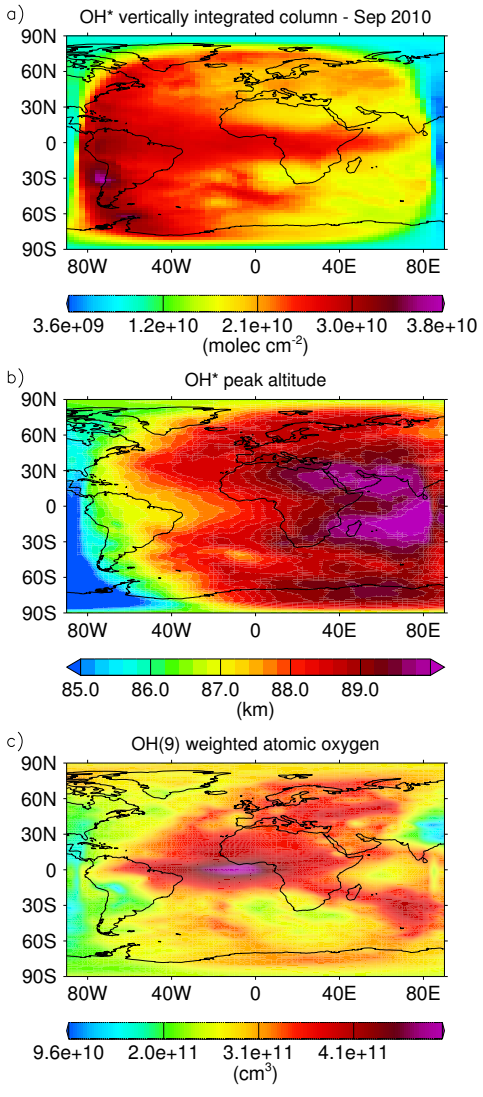


Fig. 2: Monthly averaged model results around September 2010 equinox. Panel (a): Vertically integrated number density of simulated $\sum_{i=1}^{9} \mathrm{OH}(\nu_i)$. Panel (b): Weighted peak altitudes of simulated OH emission layer according to our definition D.1. Panel (c): O concentration weighted with the OH emission layer.

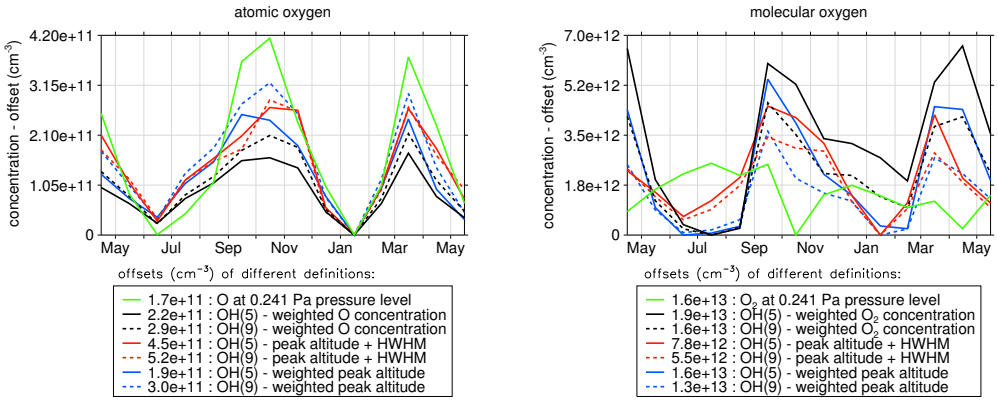


Fig. 3: Seasonal variability of simulated atomic and molecular oxygen concentrations from April 2010 to June 2011 according to the following definitions: O concentration at fixed pressure level (green line), O concentration interpolated at +HWHM shifted and weighted peak altitudes (red and blue lines), O concentration weighted with OH concentrations (black lines). From each curve the offsets listed in the legend were subtracted to allow a better intercomparison of the temporal changes.

| constant | reference | remark |
|---|---|---|
| $P$ | Adler-Golden (1997) | based on values from Steinfeld et al. (1987) |
| $A$ | Xu et al. (2012) | values based on Hitran database (Rothman et al., 2009) |
| $k_3^{O_2}$ ; $\alpha$ | Adler-Golden (1997) | based on table 2 ; $\alpha$ = correction factor from Xu et al. (2012) |
| $k_l^{N_2}$ | Adler-Golden (1997) | taken from table 1 |
| $k_l^{O}$ ; $\beta$ | Smith et al. (2010) | $\beta$ = correction factor from Xu et al. (2012) |
| $k_1$ | Sander et al. (2011) | SD-WACCM4 temperatures used for calculation of $k_1$ |

Table 1: Employed constants to Eq.(2)

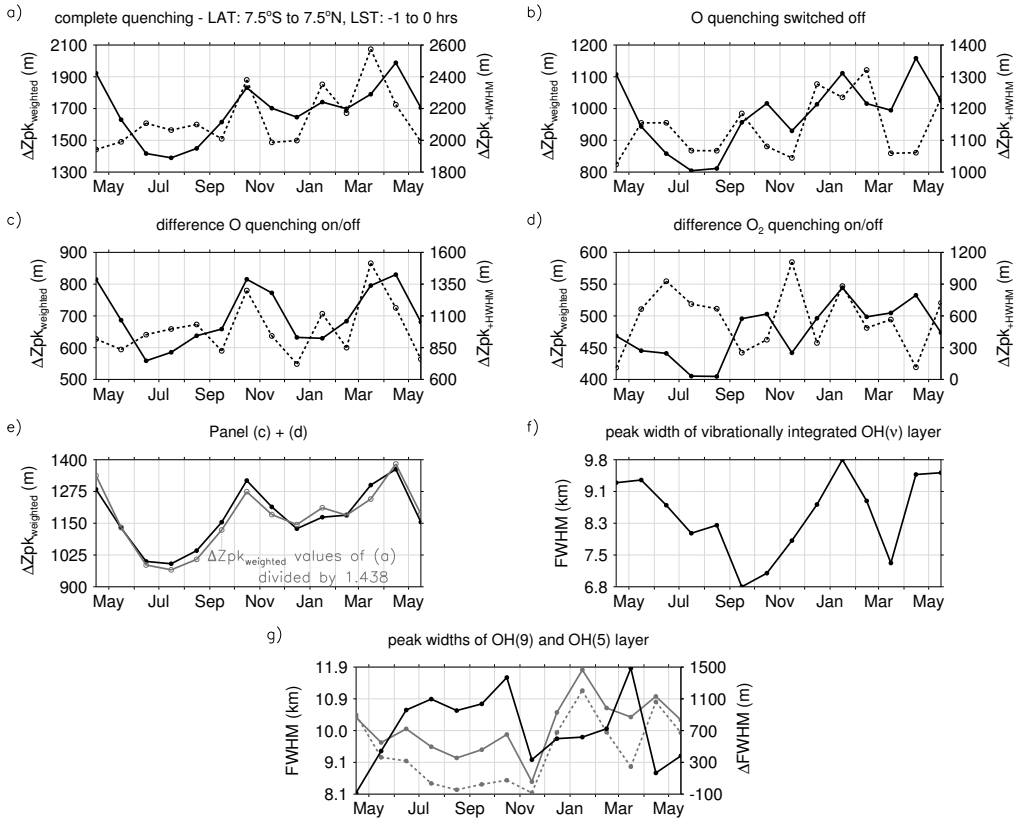


Fig. 4: Panel (a-d): Seasonal variability of vertical OH(9;5) profile shifts from April 2010 to June 2011 for different model runs within the equatorial range between $\pm 7.5^{\circ}$ and the LST range from -1 to 0 $\mathrm{hrs}$. Solid line/left axis: OH(9;5) vertical shifts between weighted peak altitudes (see definition D.1). Dashed line/right axis: OH(9;5) vertical shifts between the +HWHM shifted peak positions (see definition D.2). Panel(a): Full quenching model run. Panel(b): Deactivated O quenching model run. Panel(c): Difference in peak shifts when switching O quenching on/off. Panel(d): Difference in peak shifts when switching $O_2$ quenching on/off.Panel (e): $\{$Panel (c) + (d)$\}$ (black line). In addition, $\Delta Zpk_{\mathrm{weighted}}$ from Panel (a) divided by 1.438 shown by grey line. Panel(f): Full peak width of the vibrationally integrated OH($\nu$) layer. Panel (f)/left axis: Full peak widths of OH(9) and OH(5) layers (dashed and solid grey lines). Panel (g)/right axis: Relative difference between the full peak widths of the OH(9) and OH(5) layers (black solid line).

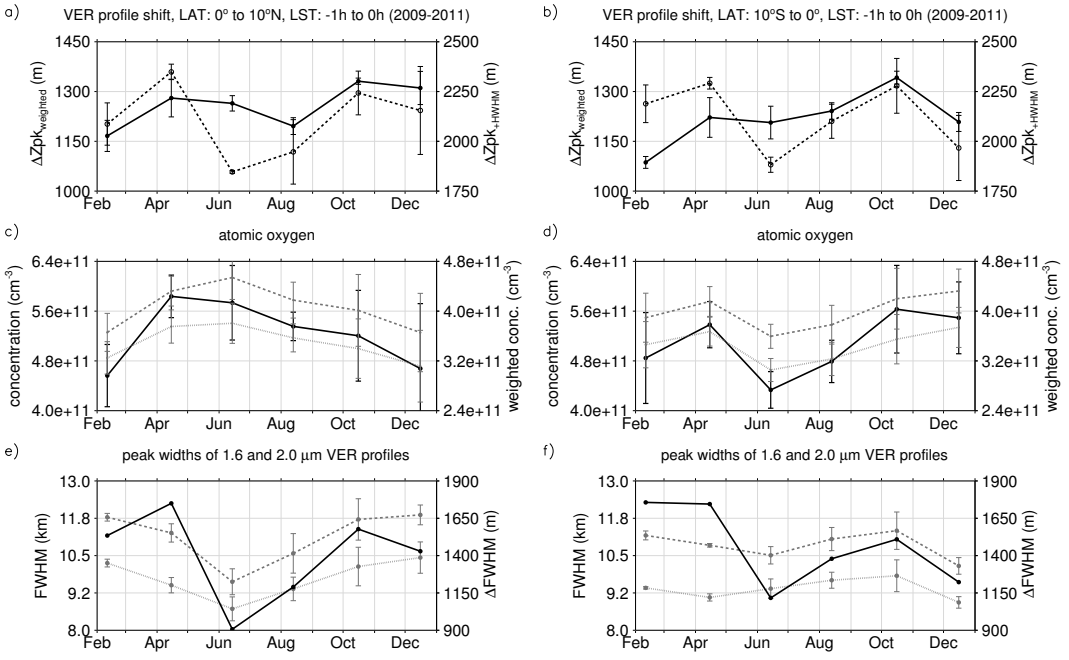


Fig. 5: SABER results based on three years of observation. Each point represents the mean value of three yaw cycles according to each year, the standard deviation is denoted by the error bars. Panel (a-b): Seasonal variability in the vertical shifts between the 1.6 and 2.0 μm VER profiles. Solid line/left axis: Vertical VER profile shifts between weighted peak altitudes according to Eq. (3). Dashed line/right axis: Vertical VER profile shifts between the +HWHM shifted peak positions according to Eq. (4). Panel (c-d): O concentrations at 90 km (left axis, black solid line) and 1.6 as well as 2.0 μm VER profile weighted atomic oxygen concentrations (right axis, dotted and dashed grey lines). Panel (e-f): Full peak widths of 1.6 and 2.0 μm VER profiles (dotted and dashed grey lines). Panel (e-f)/right axis: Relative difference between the full peak widths of the 1.6 and 2.0 μm VER profiles (black solid line).

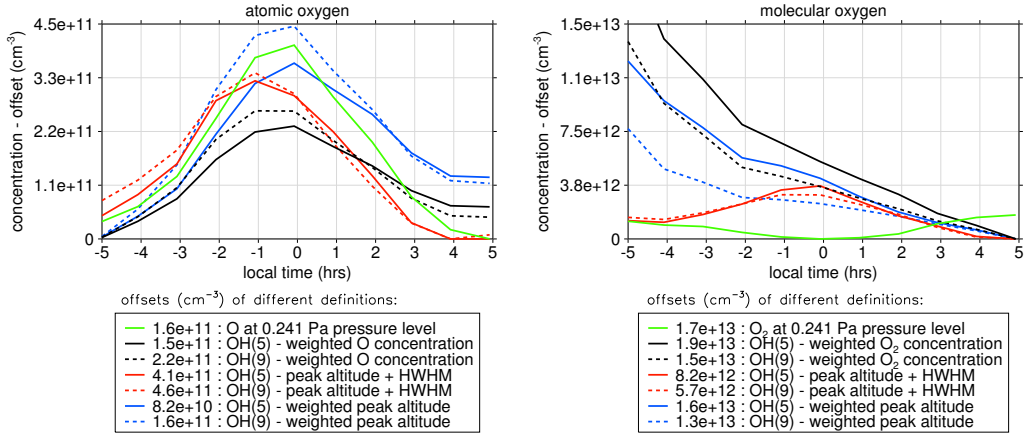


Fig. 6: Diurnal variability of simulated atomic and molecular oxygen concentrations. The same denotations apply that are used for the seasonal variability of both species in Fig. 3. The temporal averaging interval ranges from 15 September 2010 to 15 November 2010 to match the same period in our simulations that is needed for one complete SABER yaw cycle.

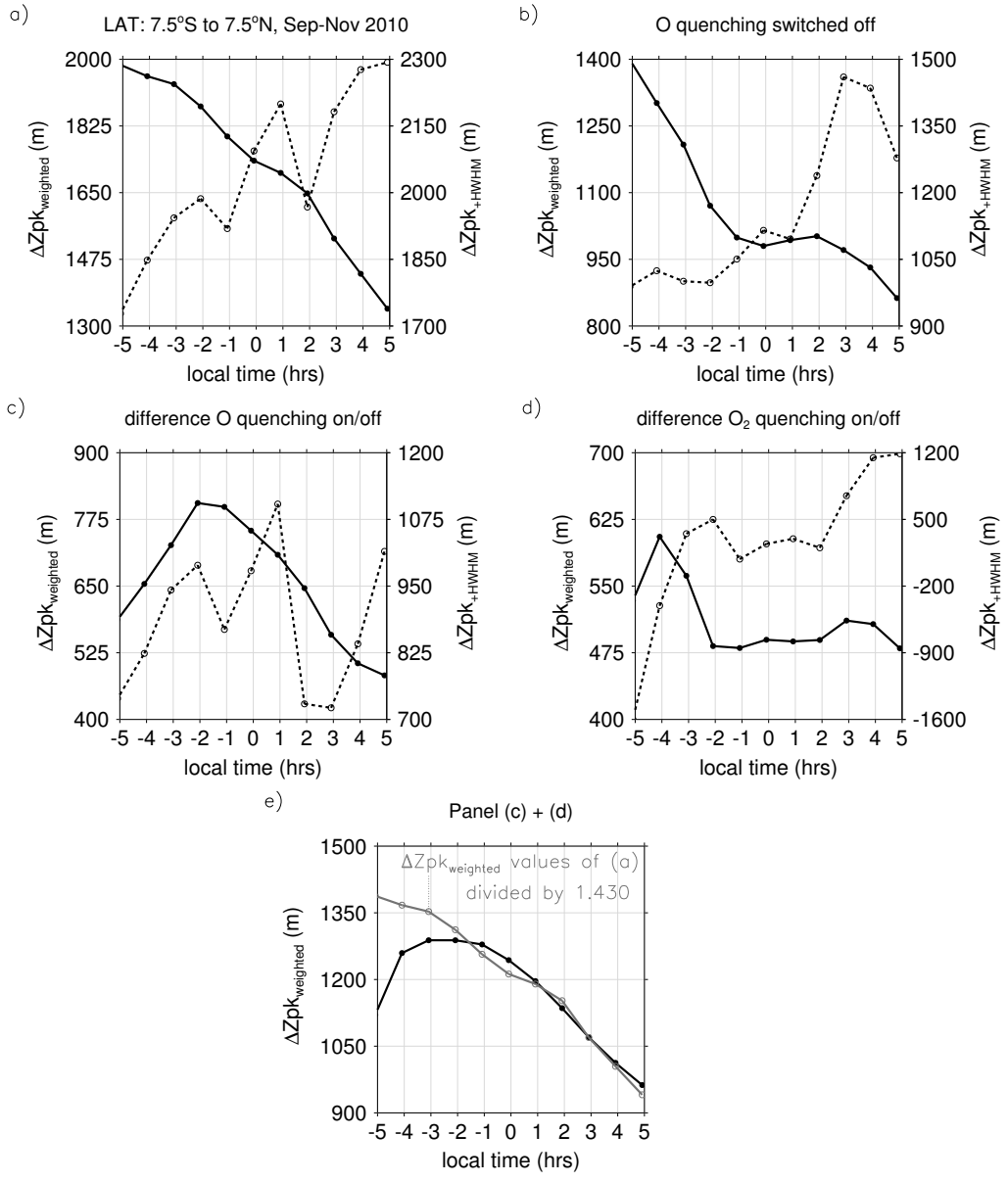


Fig. 7: Simulated diurnal evolution of vertical shifts at equatorial latitudes for the same averaging time as in Fig. 6. Panel (a): vertical shifts based on a model run including all quenching terms. The solid line refers to peak shifts with respect to weighted peak altitudes (Eq. 3), the dashed line refers to vertical shifts with respect to peak altitudes + HWHM (Eq. 4). Panel (b): peak shifts based on a model run with deactivated O quenching. Panel (c): Difference between Panel (a) and (b). Panel (c): Difference between a full quenching model run and a model run with deactivated $O_2$ quenching. Panel (e): Panel (c) + (d) (black line). Panel (f): Full peak width of the vibrationally integrated OH($\nu$) layer. Panel (f)/left axis: Full peak widths of OH(9) and OH(5) layers (dashed and solid grey lines). Panel (g)/right axis: Relative difference between the full peak widths of the OH(9) and OH(5) layers (black solid line).

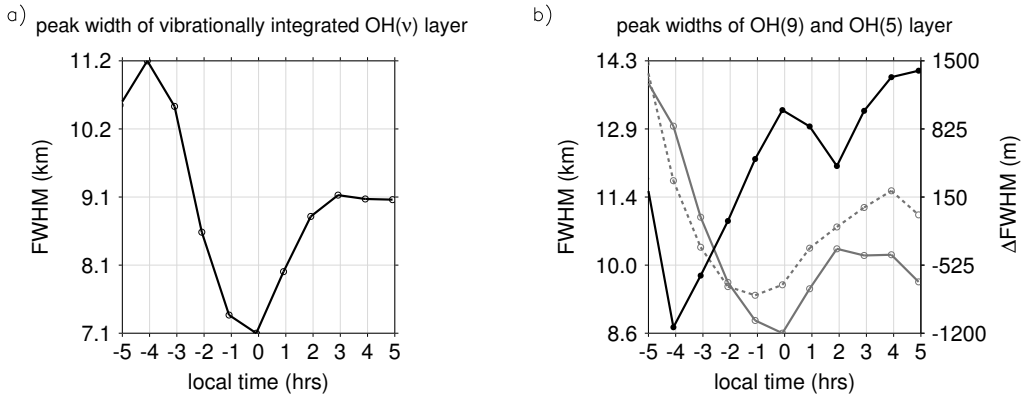


Fig. 8: Diurnal variability of OH peak widths for the same spatial and temporal bin considered in Fig. 7. Panel (a)/left axis: Full peak widths of OH(9) and OH(5) layers (dashed and solid grey lines). Panel (b)/right axis: Relative difference between the full peak widths of the OH(9) and OH(5) layers (black solid line).

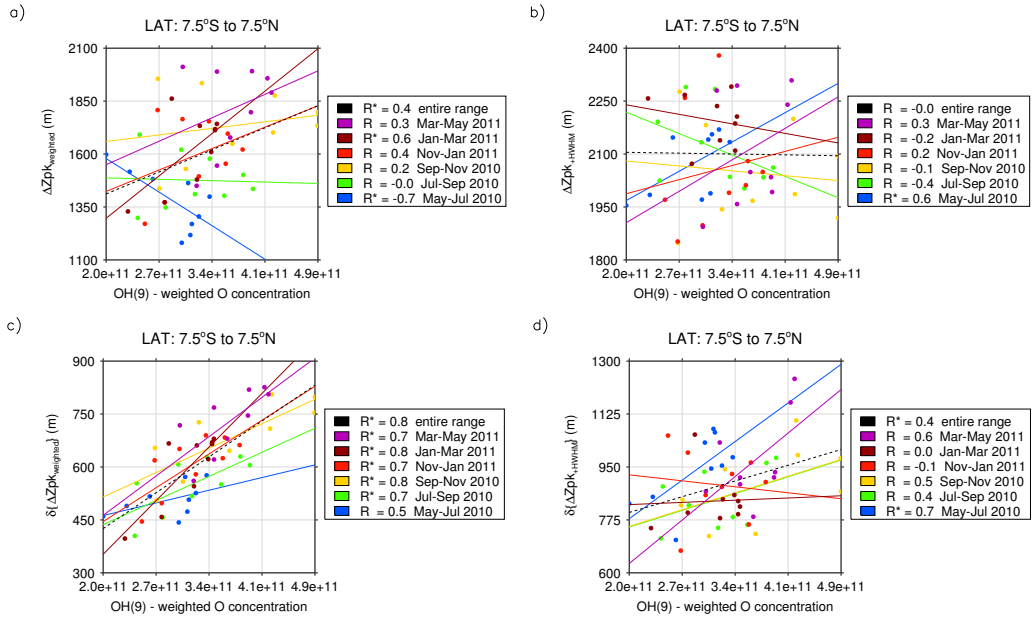


Fig. 9: Correlation plots of vertical OH(9;5) profile shifts (left panels Eq.3, right panels Eq.4) vs. OH(9) profile weighted O concentrations. The upper panels show the correlation between OH(9;5) profile shifts and O concentrations for the full quenching model run (similar to Fig. 7a). Similar to Fig. 7c, the lower panels consider the difference in vertical OH(9;5) profile shifts between the full-quenching and the deactivated O quenching model runs. Correlation coefficients are shown in the legend and denoted with the asterisk symbol *, if they were found to be significant according to a 90% significance level.

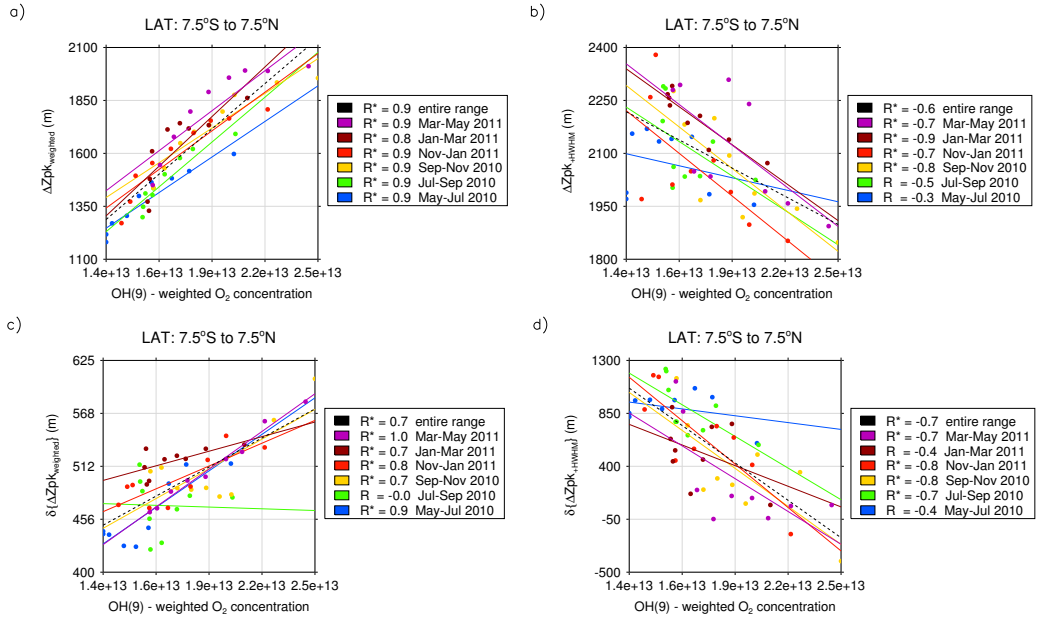


Fig. 10: Similar to Fig. 9 but referring to the $O_2$ quenching species.

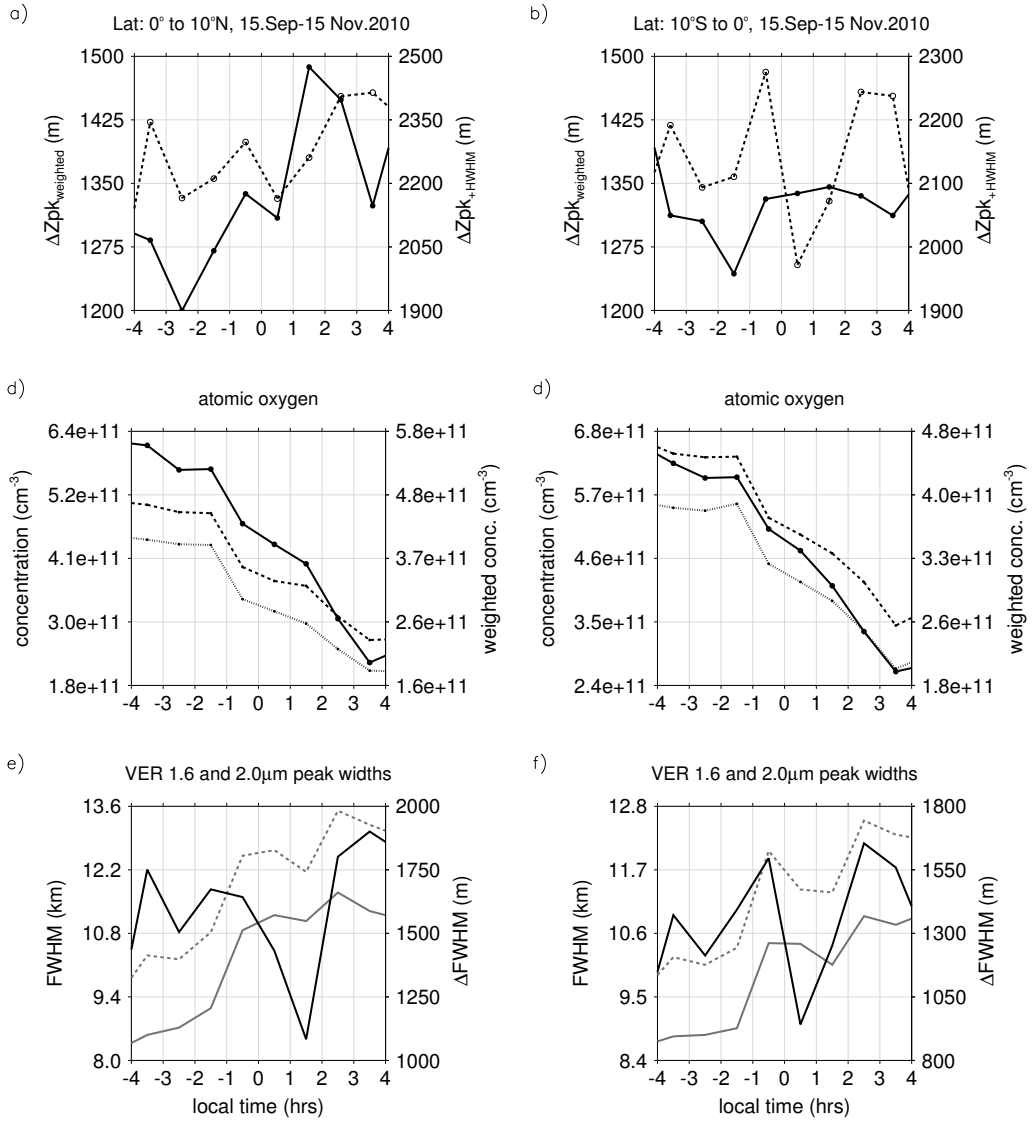


Fig. 11: Diurnal variability according to SABER OH observations. Panel (a-b): relative vertical OH peak shifts between VER($1.6\mu$m) and VER($2.0\mu$m) profiles in analogy with Fig. 7. Panel (c-d): O concentrations at 90 km level (left axis, solid line) and weighted with VER($1.6\mu$m) and VER($2.0\mu$m) (right axis, dotted and dashed line). Panel (e-f): FWHM of VER($1.6\mu$m) profile (grey dashed line), FWHM of VER($2.0\mu$m) profile (grey solid line) and the difference $\Delta$FWHM between both FWHM values (black solid line).

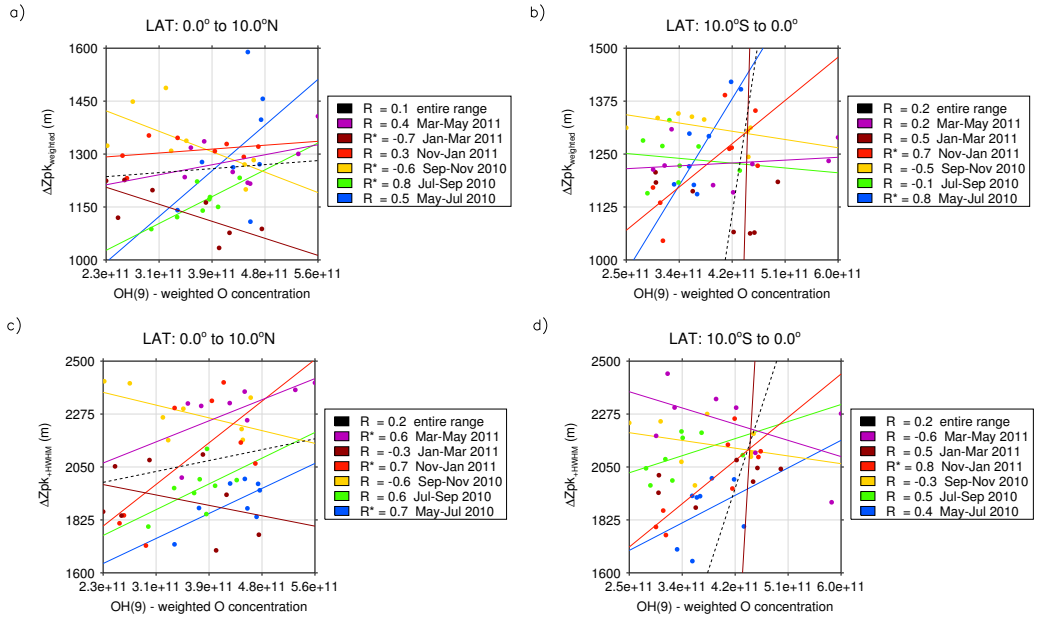


Fig. 12: Correlation between relative nighttime VER shifts and O concentrations from SABER observations in analogy with Fig. 9.